Effects of crystal orientation on the shock properties of single crystal tin

Jasper G. Threadingham,[1] Xuefei Liang,[1] Edward Leggett,[1] Liam C. Smith,[1] Jeremy C. F. Millett,[2] Glenn Whiteman,[2] Viviane Peçanha-Antonio,[3] Andrew T. Boothroyd,[3] David J. Chapman,[1] and Daniel E. Eakins[1]
[1)]*Department of Engineering Science, University of Oxford, Oxford, OX1 3PJ, UK*
[2)]*AWE, Aldermaston, Reading, RG7 4PR, UK*
[3)]*Department of Physics, University of Oxford, Oxford, OX1 3PU, UK*

(*Electronic mail: daniel.eakins@eng.ox.ac.uk)

(Dated: 21 April 2026)

Tin is known for its asymmetric crystal structure and numerous solid phase transitions, with molecular dynamics studies suggesting the beta to gamma phase transition exhibits a strong orientation dependence. In this study shock compression experiments are conducted on tin single crystals and polycrystals to probe the effects of the crystal orientation on this phase transition through Hugoniot measurements, with peak pressures between 9 GPa and 13 GPa. A strong order-of-magnitude orientation dependence of the elastic limit is found, however, the transition and post-transition behaviour show at best only qualitative differences to the velocimetry profiles, with no quantitative variation. A dependence of the transition on the peak pressure is also observed. Explanations of these results based on potential transformation pathways identified through prior static high pressure work are discussed.

I. INTRODUCTION

Sitting between the semiconductors silicon and germanium, and metallic lead in the carbon group of the periodic table, tin shares some of the complexity of the former's phase diagrams with the simplicity of the latter[1,2]. At low temperatures, tin transforms to a diamond α-phase[3], while at increasing pressures tin exhibits body centred phases (tetragonal (γ), orthorhombic and cubic) and hexagonal close-packed phases[4–7]. At ambient pressures and temperatures, tin is stable in the tetragonal phase β-tin[8,9].

The asymmetry of this tetragonal crystal structure gives rise to differences in the properties of single crystals relative to the axis tested. For instance, the compressibility[10–16] and electrical resistivity[10] of tin show significant orientation dependences, as does the thermal expansion[10,17–21], yield strength and post-yield behaviour[22]. Tin also exhibits a wide range of deformation mechanisms, such as twinning and slip[8,22–41], depending on the crystal orientation and deformation mode. The combination of these phenomena make tin an ideal candidate material for investigating and understanding the effect directionality plays on the properties of materials.

A further property of tin is the relative accessibility of the change from its ambient tetragonal β phase to a high pressure body-centred-tetragonal γ phase. This $\beta \rightarrow \gamma$ phase transition has been mapped statically, at room temperature[5,42–48], at elevated temperatures[49–52], and under normal[53–55] and oblique[56] shock loading, as seen in Figure 1. The oblique wave data by Chong *et al.* are noted for being around 10 % to 20 % lower than those from conventional shock experiments[56], although the reason for this is unclear. Isentropic compression experiments have been used to probe the transition in single crystals of orientation (100) and polycrystal samples[57], showing no significant difference. Different orientations are not, however, compared. While these studies focus on determining the conditions to induce the phase transition, more recent static tests[5,47] indicate that the phases co-exist over a range of pressures. Indeed, the static high pressure work of Fréville *et al.*[58] indicates that different crystals undergo the phase transition at different pressures during both the forward and reverse transitions. Hydrostatic pressure and temperature are therefore not the sole variables affecting the phase change. Similarly, hysteresis between forward and reverse loading has been observed in shocked polycrystals[59–61], including at elevated temperatures[62]. The double shock wave created by the transition has been experimentally measured for increasing peak pressures[63] and modelled using a mixture model where the phase transformation rate is dependent on the free energy difference between the two phases[64]. A similar model[59,65] has also been applied to the previously mentioned elevated temperature shock experiments[60,62]. While this modelling approach is well able to match the shock wave surface velocity traces, further developments are required to replicate the static findings, particularly the mixed phase region.

Tin has been studied with X-ray diffraction under shock compression[61,69–71]. This technique allows comparison between microstructure, with both Briggs *et al.*[61] and Bober *et al.*[70] finding a substantial grain size refinement across the phase transition. The cause of this phenomenon is unclear; Briggs *et al.* focus on the transition on release, while Bober *et al.* fields diffraction on jetted material, forming part of a larger body of literature examining jetting[70,72–79]. X-ray diffraction also allows for the orientation relationships between the phases to be studied. The single crystal of orientation (100) shocked by Chauvin *et al.*[71] hints at the proposed mechanism of Musgrave[80,81], although the mechanisms or post-transition microstructure cannot be conclusively established. Notably, recent diamond anvil cell work by Fréville[82] suggests two transformation pathways between the β and γ phases of tin, including the mechanism of Musgrave[80,81], depending on loading conditions, along with their respective symmetry twins.

Molecular dynamics simulations offer a potential approach to understand the behaviour of tin from the perspective of the interatomic interactions, with a number of potentials having been proposed for tin[83–90]. Perhaps the most significant, due to their ability to represent the directional nature of the bonds in tin, are the potentials of Nitol *et al.*[83], Ko *et al.*[84], and

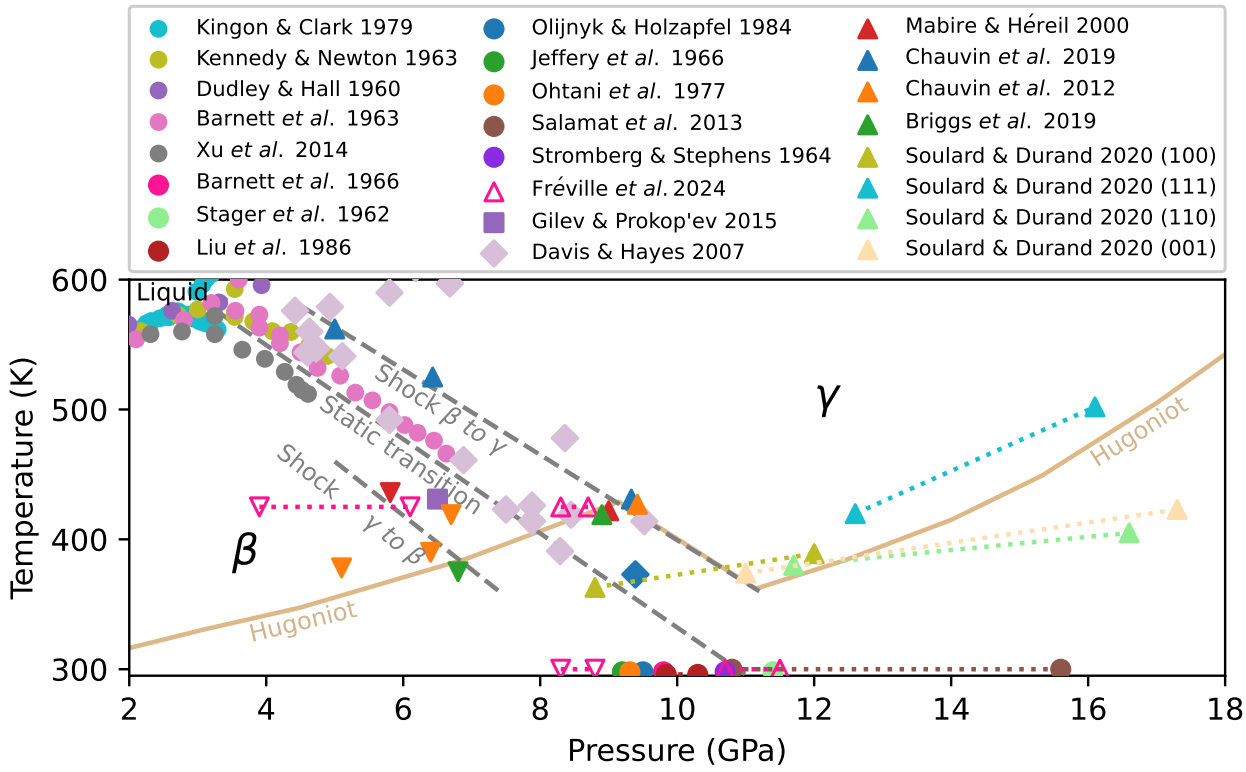

FIG. 1: Literature summary of the $\beta \rightarrow \gamma$ phase transition in tin. Circles ◯ denote static tests, squares □ denote ramp loading, diamonds ◇ denote isentropic loading, upward △ and downward ▽ triangles denote the forward and reverse transition, where filled triangles denote shock loading and unfilled triangles denote static loading. Grey dashed lines have been added as guides to the approximate location of the transition. Dotted lines denote a pressure range between which the transition takes place[5,42–52,57–62,66–68].

Baskes and Ravelo[85,86]. The former uses machine learning to optimise the potential to best represent the behaviour of tin across all phases. The potentials of Ko *et al.*, and Baskes and Ravelo, however, take a conventional embedded atom model, with modifications to better represent the directionality of the bonds in tin. These two models perform best in the α and β region, to which the potentials have been fitted. However, the Baskes and Ravelo potential has been used by Soulard and Durand[68] to model single crystals under shock loading, from the ambient β phase, through the γ phase, and up to liquid. A strong orientation dependence of the $\beta \rightarrow \gamma$ phase transition and the compressibility of the orientations below the transition is found. Given the asymmetry of the crystal properties discussed above, and the one-dimensional compression generated under shock loading, this orientation dependence is not surprising, but experimental verification is required.

Experiments to directly study the orientation dependence of the transition in tin are therefore vital to confirm whether the $\beta \rightarrow \gamma$ transition is indeed sensitive to the crystal axis along which the shock propagates. An improved understanding of this phase transition can then used as the foundation for improved modelling, from which the understanding of other materials can be developed.

II. METHODS

To probe the phase transition in single crystals of tin, a series of plate impact experiments have been conducted. A 'top-hat' geometry, Figure 2, using a C101 copper driver plate allows the shock wave to be measured as it reaches the free surfaces of both the plate and the tin sample using a double telecentric photon Doppler velocimetry (PDV) relay (more information about the experimental methods can be found in our previous work[91]). The PDV was sampled at a rate of $40\,\mathrm{GS\,s^{-1}}$ and analysed using standard short-time Fourier transform techniques[92,93] with a time window length in the range 64 to 256 depending on signal to noise ratio. Using a 50 % overlap, the time resolution for the PDV measurements is therefore ranged from 0.8 ns to 3.2 ns. The most common setting used was a 128 sample window yielding a 1.6 ns resolution.

The output PDV traces are segmented, as shown in Figure 3, to give the arrival times t_n and free surface velocities

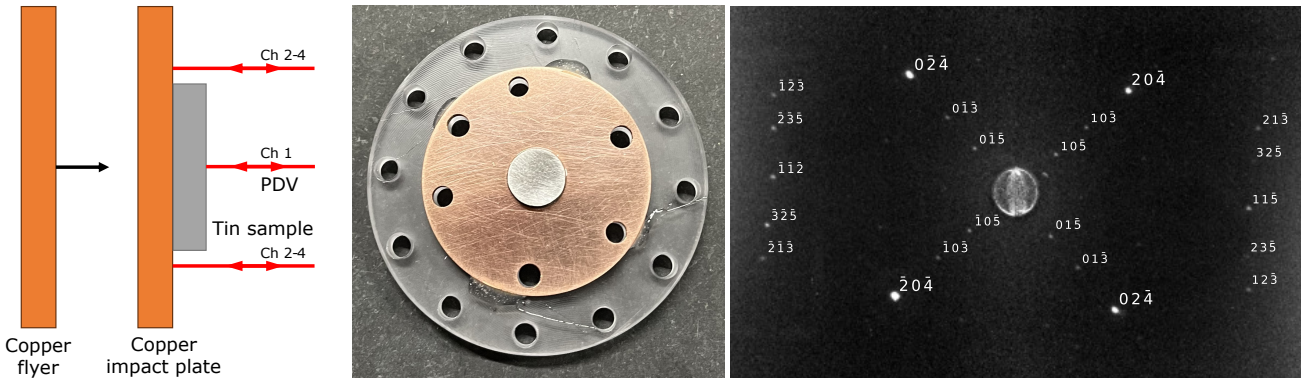

FIG. 2: Experimental geometry and target used in the plate-impact experiments. By fielding PDV on the driver plate and sample, schematic in (a), the transmission speed of shock waves can be measured as well as the free surface velocities. Samples are indexed relative to the copper plate using Laue diffraction, with the indexed diffraction pattern of sample 001_1 shown (c). Similarly the impact tilt is also determined using the radial probes as the shock breaks-out from the copper. The pattern of holes with no rotational symmetry shown in (b) is used to reference the axial rotation of both the shock tilt and the crystal.

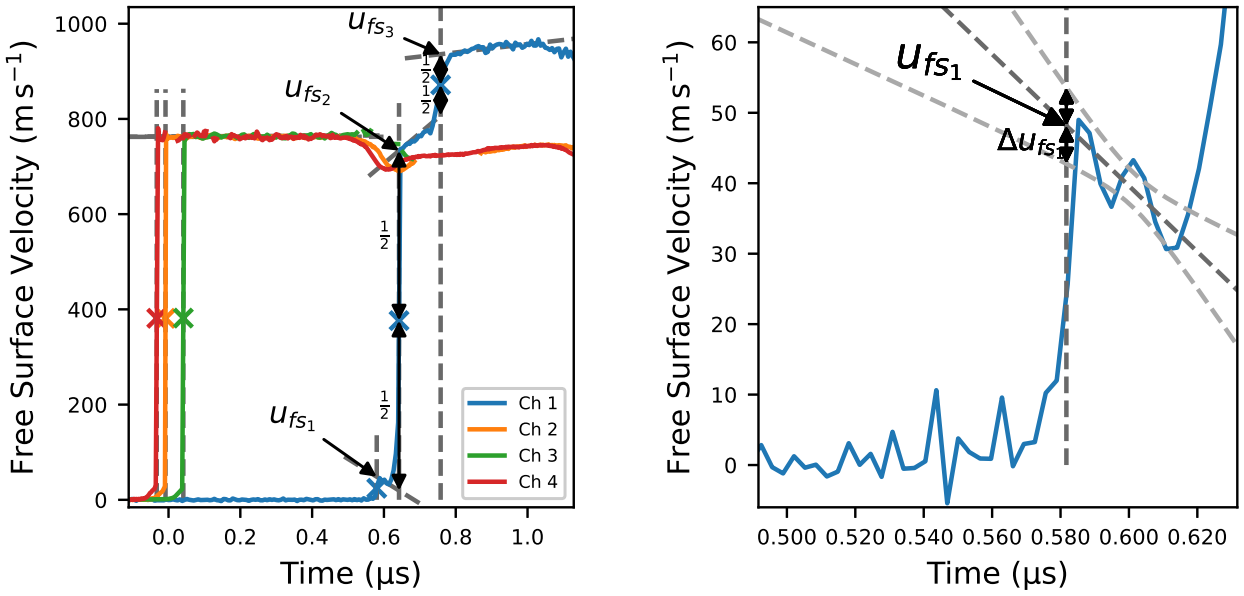

(a) Segmentation to determine wave arrival times and surface velocities u_{fs}.

(b) Uncertainty of the free surface velocity u_{fs} is determined by the 95 % confidence interval (light grey dashed lines) of the fit (dark grey dashed line.

FIG. 3: Segmentation of the velocity trace for a single crystal 110_1 to determine the free surface velocities, wave speeds and their uncertainties. The central channel (Ch 1) measures the rear surface of the tin target, while three channels (Ch 2-4) measure the surface of a copper driver plate at points distributed radially around the sample.

u_{fs_n} for each wave, following an approach similar to Barker and Hollenbach[94]. This approach divides the profile into ideal trapezoidal sections, based on fitting straight-lines to the plateaus, with vertical jumps for the arrival of each successive wave. This approach has significant advantages over other methods, such as gradient or velocity based thresholds as it can be used where the PDV signal has large noise or even drops out, as well as giving statistical uncertainties that well represent the measurements made.

The vertical jump is calculated by finding the midpoint between the adjacent plateaus, as shown in Figure 3a, thereby giving the arrival time of each wave. For almost all of the waves, especially the precursors and pre-transition waves, the time resolution of the PDV is unable to meaningfully resolve

this jump: as a result the time resolution is used as the uncertainty for most arrival times. However, where the arrival is more diffuse, uncertainty is defined by the time difference between the trace reaching the 50 % and 75 % threshold. Higher upper thresholds, or thresholds set below 50 %, would often lie in the roll-off regions. This is typically only used for the post-transition wave, such as PC_4 and PC_5 in Figure 4. The uncertainty of the arrival time is therefore given by either time difference between the 50 % and 75 % threshold, or the time resolution of the PDV analysis, whichever is greater.

The free surface velocity of each wave is extrapolated from the fit to the specified arrival time. A 95 % confidence interval computed at the arrival time is used to determine the free surface velocity uncertainty, an example of which is shown in Figure 3b. The signal noise, linearity, and degree of extrapolation are thus encapsulated within this uncertainty.

The regions for which the plateau segments are taken, from which the arrival times and free-surface velocities are calculated, are determined through a bounded brute-force optimisation where the free surface velocity uncertainty is minimised. For each possible fitting region, the fit is calculated, the arrival time of the wave determined, and the uncertainty evaluated, with the minimum uncertainty used to determine the best fit. Thus the number of fitted points, extent of extrapolation and quality of fit are all considered to analytically and repeatably segment the profiles into the various waves. Exact values and their uncertainties for the times and velocities are propagated for derived variables.

Three probes are fielded radially around the cylindrical target (Ch 2-4 in Figure 3a), from which the shock wave tilt relative to the single crystal normal can be calculated (data tabulated in Table I). The arrival time between these three channels is taken alongside the measured spot positions imaged on the target to give the entry time t_{Cu} of the shock wave into the centre of the tin sample. The Eulerian shock velocity U_{s_n} can then be deduced using

$$U_{\mathrm{s}_n} = \frac{y_n}{t_n - t_{\mathrm{Cu}}}. \tag{1}$$

Given the free surface is moving, the distance the waves travel from the driving surface to the measured free surface y_n is only the measured initial thickness y_0 for the first wave. This displacement of the free surface can be determined by integrating the free surface velocity. Assuming the free surface trace does not deviate significantly from the linear fits, a trapezium rule approach can be used, meaning the surface displacement for each subsequent wave n is given by

$$y_n = y_0 + \sum_1^n \frac{\left(u_{\mathrm{fs}_{n-1}} + u^*_{\mathrm{fs}_{n-1}}\right)}{2}\left(t_n - t_{n-1}\right), \tag{2}$$

where $u^*_{\mathrm{fs}_{n-1}}$ denotes the free surface velocity immediately before the following wave's arrival, thereby taking into account any decay or rise in the free surface velocity[95]. This correction is typically small where the waves arrive in close proximity, with a change in thickness of less than 0.5 % for the pre-transition wave and around 2 % to 3 % for the post-transition wave in the majority of samples, but can be up to 10 % for the post-transition waves in PC_4 and PC_5.

The approximation

$$u_{\mathrm{p}} = \frac{u_{\mathrm{fs}}}{2} \tag{3}$$

is used to determine the internal particle velocity u_{p}. This relies on the assumption that the release isentrope matches the loading Hugoniot. While this is not strictly true, the error introduced is small, usually less than 1 %, and systematic[95,96]. The pressure P and specific volume V for the nth wave are therefore given by the Rankine-Hugoniot conditions:

$$P_n - P_{n-1} = \rho_0 \frac{V_0}{V_{n-1}}\left(U_{s_n} - u_{p_{n-1}}\right)\left(u_{p_n} - u_{p_{n-1}}\right) \tag{4}$$

and

$$\frac{V_n}{V_0} = \frac{U_{\mathrm{s}_n} - u_{\mathrm{p}_n}}{U_{\mathrm{s}_n} - u_{\mathrm{p}_{n-1}}}\frac{V_{n-1}}{V_0}, \tag{5}$$

where the subscript 0 denotes the initial conditions[95,97].

Alongside polycrystal samples, three single-crystal orientations were tested: (100), (001) and (110). Polycrystal samples were cut from a stock bar with 5N purity and 11 mm diameter except sample PC_7 which was reduced to a 9 mm diameter. Single-crystal tin samples had a diameter of 10 mm. To determine the crystal normal relative to the driver plate, and therefore the tilt of the shock wave measured by the radial probes, the single-crystal samples were indexed using X-ray Laue diffraction, Figure 2c (rotation of crystal normal to specified direction presented in Table I). The density of the crystals was also measured. By measuring the thickness of the samples as well as the distance between the rear surface of the sample and driver plate, an indication of the glue thickness between the copper and the tin is determined. In this case, the glue layer was not resolvable by the depth gauge used, and is therefore less than the resolution of 0.01 mm.

III. RESULTS

The resulting free surface velocity traces are shown in Figure 4. The polycrystal traces are in good agreement with the literature results of Anderson *et al.*[63]. It is noted that these literature traces have been time adjusted, assuming linear dispersion rates, to account for the different thickness samples used. The pressure-volume states and shock experimental data are tabulated in Table I and plotted in Figure 5.

A. Precursor

The precursor waves in Figure 4 show considerable differences between orientations. Orientation (100), for instance, shows a precursor wave that is an order of magnitude higher than the other orientations, and significantly slower transmission speed.

TABLE I: Table of experimental and sample data.

Sample	Impact Velocity ($m s^{-1}$)	Thickness y_0 (mm)	Shock Tilt[a] Angle (mrad)	Shock Tilt[a] Rotation (rad)	Crystal Rotation[b] R_x (mrad)	Crystal Rotation[b] R_y (mrad)	Crystal Rotation[b] R_z (mrad)	Precursor C_l ($km s^{-1}$)	Precursor u_p ($m s^{-1}$)	Precursor σ (GPa)	Precursor v/v_0
100_1	775 ± 2	2.08 ± 0.01	5.0 ± 0.3	2.60 ± 0.07	-3 ± 2	871 ± 2	-3 ± 2	3.31 ± 0.04	225 ± 11	5.4 ± 0.4	0.932 ± 0.005
100_2	742 ± 1	2.08 ± 0.01	6.4 ± 0.5	-2.66 ± 0.07	3 ± 2	-1216 ± 2	-2 ± 2	3.31 ± 0.04	217 ± 8	5.2 ± 0.3	0.934 ± 0.003
001_1	777 ± 1	2.10 ± 0.01	0.3 ± 0.2	-0.84 ± 0.67	5 ± 2	717 ± 2	-5 ± 2	3.71 ± 0.04	61 ± 4	1.7 ± 0.2	0.984 ± 0.002
001_2	743 ± 3	2.06 ± 0.01	4.5 ± 0.3	-3.06 ± 0.04	-9 ± 2	-236 ± 2	-7 ± 2	3.74 ± 0.05	58 ± 6	1.6 ± 0.2	0.984 ± 0.002
110_1	765 ± 2	2.15 ± 0.01	5.2 ± 0.4	1.31 ± 0.05	0 ± 2	665 ± 2	0 ± 2	3.70 ± 0.06	24 ± 3	0.7 ± 0.2	0.993 ± 0.002
110_2	742 ± 2	2.12 ± 0.01	8.2 ± 0.5	-2.77 ± 0.06	3 ± 2	-1466 ± 2	-2 ± 2	3.63 ± 0.08	26 ± 7	0.7 ± 0.2	0.993 ± 0.002
PC_1	809 ± 2	1.92 ± 0.01	2.2 ± 0.2	-	-	-	-	3.45 ± 0.03	19 ± 2	0.5 ± 0.1	0.994 ± 0.001
PC_2	776 ± 1	1.96 ± 0.01	7.0 ± 0.5	-	-	-	-	3.46 ± 0.03	24 ± 5	0.6 ± 0.2	0.993 ± 0.002
PC_3	746 ± 2	1.85 ± 0.01	6.5 ± 0.3	-	-	-	-	3.50 ± 0.07	20 ± 5	0.5 ± 0.2	0.994 ± 0.002
PC_4	711 ± 2	1.75 ± 0.01	2.1 ± 0.3	-	-	-	-	3.44 ± 0.04	31 ± 6	0.8 ± 0.2	0.991 ± 0.002
PC_5	646 ± 2	1.84 ± 0.01	1.1 ± 0.4	-	-	-	-	3.65 ± 0.11	17 ± 5	0.5 ± 0.2	0.995 ± 0.002
PC_6	785 ± 3	2.81 ± 0.01	3.1 ± 0.3	-	-	-	-	3.52 ± 0.03	15 ± 4	0.4 ± 0.1	0.996 ± 0.002
PC_7	782 ± 1	1.00 ± 0.01	5.0 ± 0.4	-	-	-	-	3.52 ± 0.06	37 ± 2	0.9 ± 0.1	0.990 ± 0.001
PC_8	786 ± 1	1.87 ± 0.01	5.5 ± 0.4	-	-	-	-	3.61 ± 0.05	20 ± 3	0.5 ± 0.1	0.995 ± 0.001
PC_9	770 ± 5	1.96 ± 0.01	6.0 ± 0.5	-	-	-	-	3.64 ± 0.05	23 ± 10	0.6 ± 0.3	0.994 ± 0.003
PC_{10}[c]	878 ± 9	2.02 ± 0.01	3.3 ± 0.4	-	-	-	-	3.56 ± 0.06	26 ± 2	0.7 ± 0.1	0.993 ± 0.001

Sample	Density ρ_0 ($g cm^{-3}$)	Pre-transition U_s ($km s^{-1}$)	Pre-transition u_p ($m s^{-1}$)	Pre-transition P (GPa)	Pre-transition v/v_0	Post-transition U_s ($km s^{-1}$)	Post-transition u_p ($m s^{-1}$)	Post-transition P (GPa)	Post-transition v/v_0
100_1	7.28 ± 0.02	3.22 ± 0.04	380 ± 3	9.0 ± 0.2	0.884 ± 0.003	2.97 ± 0.05	474 ± 1	11.0 ± 0.2	0.852 ± 0.003
100_2	7.28 ± 0.02	3.18 ± 0.04	376 ± 6	8.9 ± 0.3	0.884 ± 0.003	2.79 ± 0.06	453 ± 2	10.4 ± 0.3	0.856 ± 0.003
001_1	7.28 ± 0.02	3.26 ± 0.04	377 ± 2	9.1 ± 0.2	0.886 ± 0.002	2.91 ± 0.11	477 ± 1	11.2 ± 0.3	0.851 ± 0.003
001_2	7.28 ± 0.02	3.26 ± 0.05	361 ± 2	8.8 ± 0.3	0.892 ± 0.003	2.74 ± 0.20	454 ± 2	10.6 ± 0.4	0.857 ± 0.005
110_1	7.28 ± 0.02	3.35 ± 0.06	367 ± 2	9.0 ± 0.3	0.891 ± 0.003	2.97 ± 0.05	463 ± 2	11.1 ± 0.3	0.858 ± 0.003
110_2	7.29 ± 0.02	3.30 ± 0.07	361 ± 5	8.8 ± 0.4	0.891 ± 0.004	2.77 ± 0.11	454 ± 3	10.6 ± 0.4	0.857 ± 0.005
PC_1	7.29 ± 0.02	3.24 ± 0.03	369 ± 4	8.8 ± 0.2	0.886 ± 0.003	2.99 ± 0.08	496 ± 1	11.5 ± 0.3	0.844 ± 0.003
PC_2	7.29 ± 0.02	3.26 ± 0.03	378 ± 3	9.0 ± 0.2	0.884 ± 0.002	2.92 ± 0.06	473 ± 2	11.0 ± 0.2	0.851 ± 0.003
PC_3	7.28 ± 0.02	3.27 ± 0.06	364 ± 2	8.7 ± 0.3	0.889 ± 0.003	2.72 ± 0.07	456 ± 2	10.5 ± 0.3	0.854 ± 0.004
PC_4	7.28 ± 0.02	3.25 ± 0.04	387 ± 1	9.2 ± 0.2	0.881 ± 0.002	2.39 ± 0.05	429 ± 1	9.9 ± 0.2	0.863 ± 0.003
PC_5[d]	7.29 ± 0.02	3.26 ± 0.04	380 ± 1	9.1 ± 0.2	0.884 ± 0.002	2.15 ± 0.09	411 ± 1	9.5 ± 0.2	0.868 ± 0.003
PC_6	7.29 ± 0.01	3.34 ± 0.02	378 ± 2	9.2 ± 0.1	0.887 ± 0.001	3.00 ± 0.06	478 ± 1	11.4 ± 0.2	0.853 ± 0.002
PC_7	7.29 ± 0.02	3.28 ± 0.06	384 ± 2	9.2 ± 0.3	0.884 ± 0.003	2.89 ± 0.08	478 ± 1	11.2 ± 0.3	0.850 ± 0.004
PC_8	7.29 ± 0.02	3.36 ± 0.04	374 ± 2	9.2 ± 0.2	0.889 ± 0.002	3.00 ± 0.07	483 ± 2	11.6 ± 0.3	0.852 ± 0.003
PC_9	7.29 ± 0.02	3.36 ± 0.04	385 ± 3	9.5 ± 0.3	0.886 ± 0.003	2.98 ± 0.06	466 ± 2	11.2 ± 0.3	0.858 ± 0.003
PC_{10}[c]	7.29 ± 0.02	3.32 ± 0.04	390 ± 99	9.5 ± 2.6	0.883 ± 0.031	3.29 ± 0.06	536 ± 7	13.0 ± 0.4	0.839 ± 0.005

[a] Shock tilt angle is given by the angle between the normal of the shock plane and the normal of the driver plate (y axis). The rotation is given as the rotation of the normal of the shock plane projected onto the driver plate, positive taken as clockwise from the vertical (z axis), defined by the mirror symmetry of the target (see Figure 2b)

[b] Crystal rotation is given as the angle of the specified orientation relative to the normal to the driver plate (y axis). The x axis is horizontal, while the z axis is the vertical axis formed by the mirror symmetry (see Figure 2b).

[c] Re-analysis of the data presented in[91]. The pre-transition step is only measurable with high time resolution analysis, resulting in low statistical confidence for this measurement.

[d] Phase transition incomplete. Post-transition state taken as highest state reached before spall.

The polycrystal precursor pressure is found to be somewhat larger than other Hugoniot elastic limit (HEL) literature values. For example, Mabire reports around 0.2 GPa[65], although the use of VISAR tuned to the phase transition may be less sensitive to the HEL. Similarly, Steinberg[104] reports a value of 0.24 GPa. The provenance of this is unclear, however, this value is similar to the value of 0.194 GPa found in ramp-wave tests[56]. Indeed, laser shock experiments at a much higher strain-rate indicate a value in excess of 1 GPa[105] and free surface velocities around $100\,m s^{-1}$[106]. The strain-rates for these various measurements cannot be numerically compared, although the strain-rate of the shock experiments conducted here would be expected to sit towards the centre of the range of literature strain-rates, with the measured HEL reflecting this intermediate position. Notably the results presented here are good agreement with the particle velocity measurements in the plate-impact experiments of Anderson *et al.*[63].

The wave speed of this polycrystal precursor is a little faster than the ambient longitudinal sound speed of $3.43\,km s^{-1}$ given by Marsh[98]. Notably the polycrystal sound speed is consistent with the sound speed of $3.54\,km s^{-1}$ measured at 300 K and 0.75 GPa[52]. Similarly, the single-crystal wave speeds are

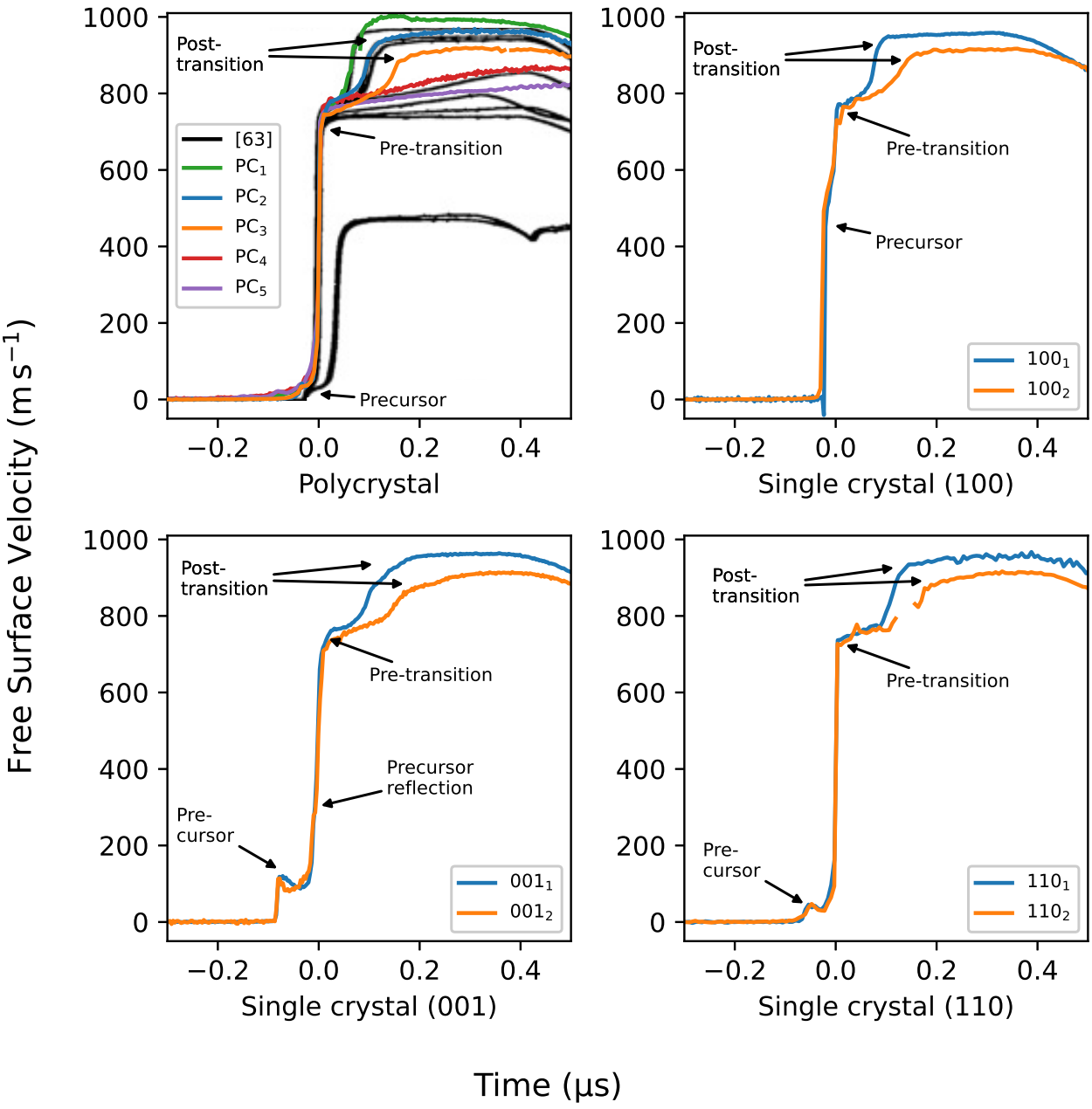

FIG. 4: Rear surface velocity traces for plate impact experiments on a range of tin samples. Key features are indicated. Polycrystal data is in good agreement with the free surface velocity traces of Anderson *et al.*[63] (black lines), reproduced from W. W. Anderson *et al.*, "Phase transition and spall behavior in β-tin," in Shock Compression of Condensed Matter - 1999 (AIP Publishing, 2000) pp. 443–446, with the permission of AIP Publishing. Times referenced to pre-transition wave.

faster than ambient ultrasonic velocity measurements determined using the pulse-echo technique[107], see Table II. Orientation (100) exhibits the slowest sound speed under both shock and ambient conditions. However, while (110) and (001) have similar ambient longitudinal wave speeds, under shock loading, where (001) exhibits a significantly greater compression, the wave speed in (001) is larger. This observation implies, given the elastic longitudinal wave speed correlates with square root of the elastic modulus, the material stiffens with increasing stress.

Indeed, the apparent stiffness C can be calculated using the wave speed through

$$C = \rho_0 U_s^2. \tag{6}$$

The resulting apparent stiffness is presented in Table III, compared to literature second order coefficients[14]. The second order coefficients clearly underestimate the stiffness, suggesting a third order model, where the material stiffness increases as

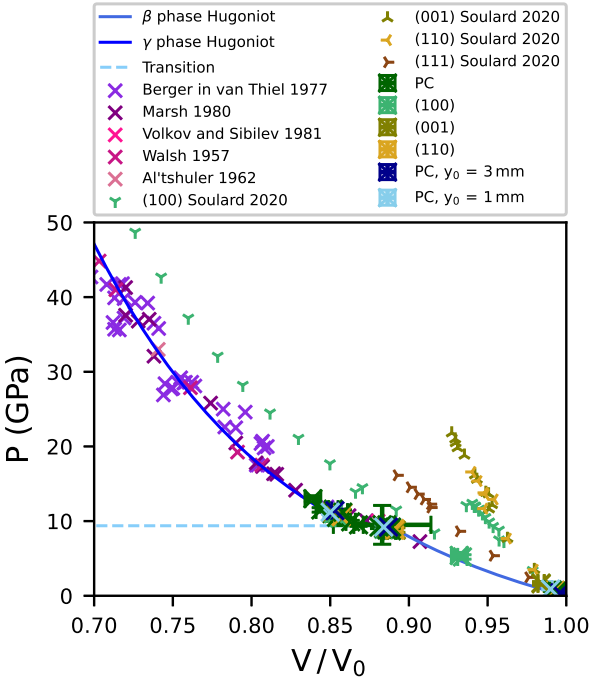

FIG. 5: Pressure-volume data determined in this work compared to literature values[68,98–103]. Hugoniot and transition calculated from the Birch-Murnaghan model determined by Mabire and Héreil[59].

TABLE II: Elastic longitudinal wave speeds in single crystal tin measured at ambient conditions and under shock.

Orientation	Ambient conditions[107]	Shock - this study
(001)	3.446 ± 0.015	3.71 ± 0.04
	3.430 ± 0.010	3.74 ± 0.05
(100)	3.112 ± 0.015	3.31 ± 0.04
		3.31 ± 0.04
(110)	3.481 ± 0.018	3.70 ± 0.06
		3.63 ± 0.08

the material is compressed, should be used. For each orientation, the principal stress σ in the direction of the wave is given by[108]

$$\sigma_{100} = -\frac{V}{V_0}\eta\left(C_{11} + \frac{\eta}{2}C_{111}\right), \tag{7a}$$

$$\sigma_{001} = -\frac{V}{V_0}\eta\left(C_{33} + \frac{\eta}{2}C_{333}\right), \tag{7b}$$

and

$$\sigma_{110} = -\frac{\eta}{2}\frac{V}{V_0}\left(C_{11} + C_{12} + 2C_{66} + \frac{\eta}{4}\left(C_{111} + 3C_{112} + 12C_{166}\right)\right) \tag{7c}$$

TABLE III: Table of elastic data

Sample	Stiffness $\rho_0 {U_s}^2$ (GPa)	Second order Coefficient	Value[14] (GPa)
100_1	79.8 ± 1.9	C_{11}	72.30
100_2	79.6 ± 1.6		
001_1	100.4 ± 2.1	C_{33}	87.4
001_2	101.9 ± 2.7		
110_1	99.9 ± 3.2	$\frac{1}{2}(C_{11} + C_{12} + 2C_{66})$	89.85
110_2	96.0 ± 3.8		

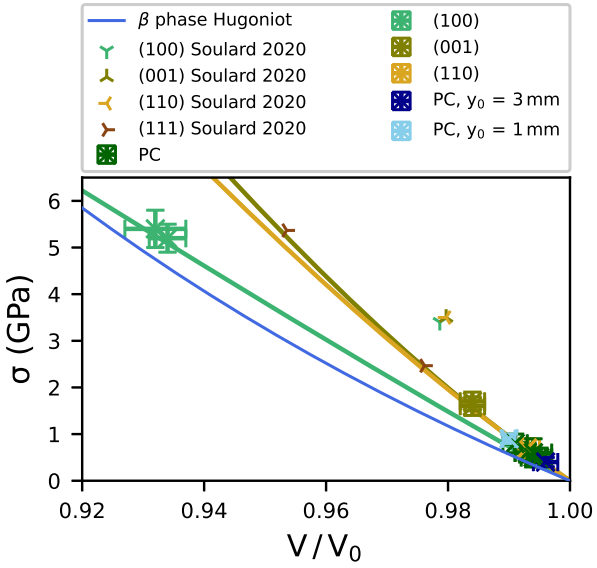

FIG. 6: Precursor data plotted against a third order elastic stress-strain model (solid lines, same colour as experimental data of the same orientation)[108]. Second order parameters from Rayne and Chandrasekhar[14], third order from Swartz *et al.*[107]. Hugoniot for the β phase calculated from the Birch-Murnaghan model of Mabire and Héreil[59]. Single-crystal molecular dynamics simulation states by Soulard and Durand[68] are included for comparison.

where

$$\eta = \frac{1}{2}\left(\left(\frac{V}{V_0}\right)^2 - 1\right). \tag{8}$$

Plotting these third order approximations in Figure 6 with second order coefficients from Rayne and Chandrasekhar[14] and third order coefficients from Swartz *et al.*[107] fits the measured data well. Thus, the strain-rate dependence on the elastic properties is likely indirect, with increasing strain-rate increasing the threshold for plasticity, resulting in a larger magnitude, and, therefore, faster, elastic wave propagating in the material.

The agreement with the elastic model and statically determined wave speeds lends confidence to the conclusion that the

precursor waves are indeed elastic. However, this does not explain the magnitude of the waves, especially in the (100) orientation. An unusually high precursor was reported by Davis and Hayes[57] in isentropic compression tests of (100) orientation single crystals, although "bond-layer thermal distortions" was the hypothesised cause. It is noted that applying compressive low-energy impact loads along the [100] direction drives plastic deformation through twinning[41]. The high pressure plastic behaviour of tin has been suggested to be dominated by twinning in split-Hopkinson pressure bar, pulsed power driven ramp, hole closure, Richtmyer-Meshkov instability and Taylor cylinder tests[109]. At cryogenic temperatures, this orientation is also found to fail without plasticity at a significantly higher pressure than other orientations[22], suggesting that twinning may require large stresses to initiate in time- or energy-constrained conditions in this orientation.

An estimation of the internal stresses in the samples at the precursor state, the state where the properties diverge from the predicted single-crystal elastic compression curve, can be determined using the previously mentioned third order elastic model. By taking the mean of the uniaxial strain at the precursor for the two tests per orientation, the stress field can be calculated, from which the resolved shear stress for the potential slip and twinning systems in tin can be estimated (detail in the Appendix). Seven slip systems have been experimentally observed in tin[8,22–38], alongside two twin systems[39–41], tabulated in Table IV. Critical shear stresses are somewhat uncertain and incomplete for these slip systems. Typical values are around or slightly below 1 MPa[22–24,41]. Other systems have been proposed[29,34,110,111], however measurements are scarce and observations inconsistent between sources. While it may be possible that these additional systems occur under specific loading and temperature conditions, only the core seven systems that are repeatedly observed are used for this analysis[22,112,113]. The results of this analysis are presented in Table IV.

It can be seen that more slip systems experience shear in the (110) orientation than the other orientations. The magnitude of the shear stresses for all systems is also lower in (110) than for the other tested orientations, while still being an order of magnitude larger than the critically resolved shear stresses determined for quasi-static conditions[22–24]. While rate effects may explain the rise in critically resolved shear stress, an order-of-magnitude rise is perhaps unexpected. Orientation (100) shows the highest resolved shear stresses, especially in the twinning systems. Notably, all the systems show a higher stress than in the (001). Assuming a simple Schmid model where the slip or twinning system activates when a critical stress is reached, any system that activates in (001) should activate well before reaching the HEL state measured in (100). A single critical value of resolved shear stress cannot therefore predict the onset of plasticity, and given the elastic anisotropy, factors such as strain-rate and elastic potential energy may give better insights. Behaviour more complicated than a classical activation stress model is therefore observed, and warrants further study.

TABLE IV: Shear stress in GPa resolved for each slip system and crystal direction at the precursor state.

Slip system	Shock Orientation		
	(100)	(001)	(110)
$(1\,0\,0)[0\,0\,1]$	0	0	0
$(0\,1\,0)[0\,0\,1]$	0	0	0
$(1\,1\,0)[0\,0\,1]$	0	0	0
$(1\,\bar{1}\,0)[0\,0\,1]$	0	0	0
$(1\,1\,0)[1\,\bar{1}\,1]$	0.20	0	0
$(1\,1\,0)[\bar{1}\,1\,1]$	0.20	0	0
$(1\,\bar{1}\,0)[1\,1\,1]$	0.20	0	0
$(1\,\bar{1}\,0)[\bar{1}\,\bar{1}\,1]$	0.20	0	0
$(1\,0\,1)[1\,0\,\bar{1}]$	0.91	0.39	0.09
$(\bar{1}\,0\,1)[1\,0\,1]$	0.91	0.39	0.09
$(0\,1\,1)[0\,\bar{1}\,1]$	0.69	0.39	0.09
$(0\,\bar{1}\,1)[0\,1\,1]$	0.69	0.39	0.09
$(1\,2\,1)[1\,0\,\bar{1}]$	0.66	0.28	0.17
$(\bar{1}\,2\,1)[1\,0\,1]$	0.66	0.28	0.04
$(1\,\bar{2}\,1)[1\,0\,\bar{1}]$	0.66	0.28	0.04
$(\bar{1}\,\bar{2}\,1)[1\,0\,1]$	0.66	0.28	0.17
$(2\,1\,1)[0\,\bar{1}\,1]$	0.48	0.28	0.17
$(\bar{2}\,1\,1)[0\,\bar{1}\,1]$	0.48	0.28	0.04
$(2\,\bar{1}\,1)[0\,1\,1]$	0.48	0.28	0.04
$(\bar{2}\,\bar{1}\,1)[0\,1\,1]$	0.48	0.28	0.17
$(1\,0\,0)[0\,1\,0]$	0	0	0.18
$(0\,1\,0)[1\,0\,0]$	0	0	0.18
$(1\,0\,0)[0\,1\,1]$	0	0	0.15
$(1\,0\,0)[0\,\bar{1}\,1]$	0	0	0.15
$(0\,1\,0)[1\,0\,1]$	0	0	0.15
$(0\,1\,0)[1\,0\,\bar{1}]$	0	0	0.15
$(3\,0\,1)[\bar{1}\,0\,3]$	0.90	0.42	0.10
$(\bar{3}\,0\,1)[1\,0\,3]$	0.90	0.42	0.10
$(0\,3\,1)[0\,\bar{1}\,3]$	0.74	0.42	0.10
$(0\,\bar{3}\,1)[0\,1\,3]$	0.74	0.42	0.10

B. Phase Transition

While these precursor waves show significant orientation dependence, the pre- and post-transition states show only qualitative differences. For instance, the transition waves of (001) appear to roll-off more than the other orientations, as shown in Figure 4, while (110) shows a much more angular profile. The profile of the post-transition wave in (001) could be indicative of a phase interface reflection, similar to that seen in iron[94]. Why this effect is orientation dependent is unclear, but could be tied to the elastic properties. However, the pressures and volumetric compressions appear to be clustered between the different orientations in Figure 7, without exceeding the experimental uncertainty. Consequently, any orientation dependences are likely to be small, if present at all.

The spread of impact velocities gives an insight into the possible pressure relationship of the transition. As plotted in Figure 8 alongside literature data, a linear relationship of the form

$$P_{\text{transition}} = mP_{\max} + c \tag{9}$$

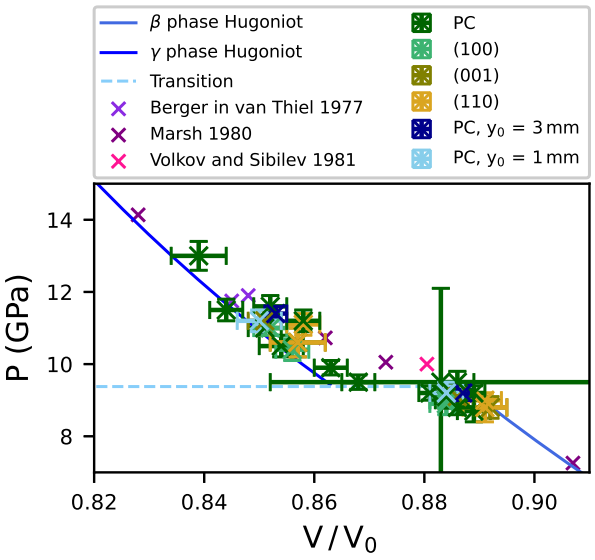

FIG. 7: Pressure-volume data for the pre- and post-transition states plotted alongside literature values[98,99,103]. Hugoniot and transition calculated from the Birch-Murnaghan model determined by Mabire and Héreil[59].

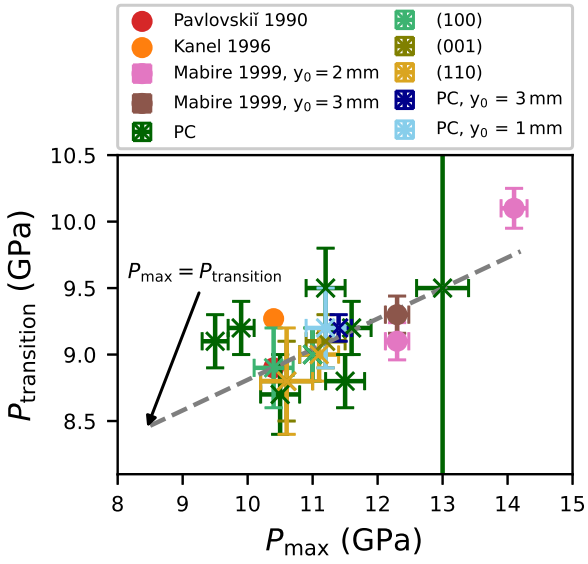

FIG. 8: Comparison between the pre-transition wave pressure to the peak pressure state, including literature values[55,65,114]. A linear fit is taken (grey-dashed line).

between the peak pressure and the pre-transition pressure is proposed.

To test this hypothesis a reduced χ^2 statistical test is conducted on the data presented in Table I. Given the experimental uncertainties,

$$\chi^2 = \sum \frac{(P_{\text{transition}} - (mP_{\text{max}} + c))^2}{\Delta P^2_{\text{transition}} + (m\Delta P_{\text{max}})^2} \tag{10}$$

estimates of the quality of the fit by taking the ratio of the distance of the data-points from the line of best fit to their measured uncertainties. As a result, after dividing by the degrees of freedom (dof; the number of data points minus the number of fitting parameters), a good fit should reach a value close to unity. If the data deviates significantly from the proposed fit, the experimental uncertainties will be smaller than the deviation from the fit, meaning χ^2/dof would be much larger than one, and similarly if the uncertainties are larger than the deviation, χ^2/dof would be much smaller than one.

To determine the optimal fit, equation (10) is minimised. Data from Mabire[65] are included in the fit, though it is noted that their uncertainties are blanket percentages, and may not therefore represent the individual experimental measurement. The resulting relationship is found to be

$$P_{\text{transition}} = 0.23P_{\text{max}} + 6.51, \tag{11}$$

where both the gradient m and the intercept c are quoted to two decimal places, and in units of GPa for the intercept. An implication of this equation is that the minimum transition pressure, when the maximum pressure is equal to the transition pressure, is 8.5 GPa. This is between the values for an unstrained (8.7 GPa) and strained (8.3 GPa) crystal determined statically at a temperature corresponding with the approximate Hugoniot temperature by Fréville *et al.*[58]. The upper bound can be found by graphically applying the Rayleigh condition, yielding around 15 GPa. The value of χ^2/dof is found to be 1.3. This suggests the uncertainties are slightly underestimated, should the proposed fit be valid, especially given the lower uncertainties presented by Mabire and the large uncertainty of the transition state due to the small step in experiment PC_{10}. Further shock tests are required to better explore this relationship, especially to probe the minimum threshold pressure as well as measure the influence of other variables, such as initial sample temperature.

Modelling the transition using a transformation rate dependent on the Gibbs energy difference between the two phases, such as that by Cox and Robinson[64], has replicated the velocity profiles presented in Anderson *et al.*[63] that are indicative of the pressure dependence of the transition. A similar approach by Chong *et al.*[56], supported by oblique ramp-wave experiments, shows a decay in the pre-transition wave with the thickness of the sample. The data analysed here does not replicate this effect. From the thickest samples, 6 mm and 9.15 mm from Pavlovskiĭ and Komissarov[55], to the thinnest, no significant deviations from the fit are visible.

IV. DISCUSSION AND CONCLUSION

Through plate-impact shock experiments, the complex behaviour of tin has been unveiled. The precursor waves map

well to elastic compressibility, but the plastic transition shows an unexpected order-of-magnitude difference between single-crystal orientations. Resolving the state at the peak of this precursor indicates that a simple Schmid model of critical shear stress does not well describe this behaviour. The causes of this phenomenon are unclear, however it is noted that (100) has the highest compressibility, and therefore it is possible that the strain-rate is significantly higher in this orientation than in the other orientations. Although the strain-rate is too fast to be accurately measured with the current PDV system, increasing the strain-rate would be expected to increase the threshold required to slip or twin, especially if the change in strain-rate were to move into the phonon-drag regime. Higher time resolution diagnostics to measure the corresponding strain-rate of these waves may shed some light on any link between the yield and strain-rate.

These experiments also cannot diagnose the exact mechanisms of plasticity. To confirm the plastic mechanisms that act at these high-rates, further experiments are required, such as shock recovery experiments. Further experiments and modelling are therefore required to better understand the phenomenon underpinning the elastic-plastic transition in tin.

While some qualitative differences are evident between the phase transitions in the different orientations, the experimental uncertainties are such that no statistically significant differences can be established. Consequently, it is concluded that there is a large orientation dependence of the HEL, above which there is not a significant orientation dependence of the properties. This is in contrast to previous molecular dynamics simulations[68], Figure 5, although it is acknowledged that the strain-rates an sample volumes differ by many orders of magnitude. Indeed, considering Figure 6, some orientations follow the elastic compressibility curves, suggesting further refinements to the potentials are needed to better represent tin under shock loading.

Given that multiple transition pathways have been detected statically[82], it is hypothesised that multiple transformations of different pathways are initiated under shock loading. A variety of mechanisms may explain the qualitative differences between free surface velocity profiles (Figure 4), with different mechanisms being associated with different transformation rates. In addition, due to the reduction in density across the phase change, residual stresses will be generated at the interaction boundaries of these regions. These residual stresses will then further perturb the original post-transition orientation, leading to a broad distribution of polycrystalline orientations, with modes centred around an unperturbed post-transition orientation. Thus single-crystal samples form a much finer microstructure across the transition; the results of Morgan *et al.*[115], Briggs *et al.*[61] and Bober *et al.*[70].

Alternatively, the lack of orientation dependence may lie with shock-induced recrystallisation prior to the phase transition. The proximity to melt may allow recrystallisation to occur after the HEL is reached[116], thereby losing any initial orientation relationship. Whilst verifying these hypotheses remains a challenge, *in situ* X-ray diffraction and soft recovery of shocked samples offer potential methods to study this phenomenon. These methods could help build a better understanding of the pre-transition plastic behaviour.

A plate impact study has been performed on single-crystal tin to investigate the role of crystal orientation on the shock response. The HEL was observed to show a significant anisotropy of wave speed, compressibility and magnitude. Above this limit, the phase transition shows some qualitative differences but no quantitative variation between orientations. This behaviour points towards microstructural changes, notably plastic phenomenon such as recrystallisation as well as phase-transformation kinetics, eradicating any sample orientation effects. Further experimentation and modelling, such as sub-transition plate-impact tests, shock-recovery or *in situ* high-rate X-ray diffraction experiments, as well as molecular dynamics simulations, are therefore required to better understand these phenomena. Through this enhanced understanding and modelling capability, a better understanding of other materials may be developed.

V. ACKNOWLEDGEMENTS

The authors gratefully acknowledge AWE for their continued support. Thanks also to Stuart Carter and the ISML workshop for their help manufacturing samples and consumables. Thanks to Martí Puig Fantauzzi for valuable conversations regarding molecular dynamics models of tin.

VI. AUTHOR DECLARATIONS

A. Conflicts of Interest

The authors have no conflicts to disclose.

B. Author Contributions

Jasper G. Threadingham: Conceptualisation (lead); Data curation (lead); Formal analysis (lead); Investigation (lead); Methodology (lead); Writing – original draft (lead); Writing – review & editing (lead). **Xuefei Liang**: Investigation (equal). **Edward Leggett**: Investigation (equal); Writing – review & editing (equal). **Liam C. Smith**: Investigation (equal); Writing – review & editing (equal). **Jeremy C. F. Millett**: Conceptualisation (supporting); Funding acquisition (equal) Resources (equal); Supervision (supporting). **Glenn Whiteman**: Conceptualisation (supporting); Funding acquisition (equal); Resources (equal); Supervision (supporting). **Viviane Peçanha-Antonio**: Methodology (supporting); Resources (supporting). **Andrew T. Boothroyd**: Methodology (supporting); Resources (supporting); Writing – review & editing (supporting). **David J. Chapman**: Conceptualisation (equal); Funding acquisition (equal); Investigation (equal); Supervision (equal); Writing – review & editing (equal). **Daniel E. Eakins**: Conceptualisation (equal); Funding acquisition (lead); Investigation (equal); Supervision (lead); Writing – review & editing (equal).

C. Data Availability

The data that support the findings of this study are available from the corresponding author upon reasonable request.

VII. REFERENCES

[1] F. P. Bundy, "Phase diagrams of silicon and germanium to 200 kbar, 1000°C," The Journal of Chemical Physics **41**, 3809–3814 (1964).

[2] N. A. Smirnov, "Ab initio calculations of the phase diagrams of tin and lead under pressures up to a few TPa," Journal of Physics Condensed Matter **33** (2021), 10.1088/1361-648X/abbbc5.

[3] I. N. Nikolaev, V. P. Mar'in, V. N. Panyushkin, and L. S. Pavlyukov, "Characterisation of the alpha → beta tin phase transformation under pressure," Soviet Physics Solid State **14**, 2337–2339 (1973).

[4] A. Salamat, G. Garbarino, A. Dewaele, P. Bouvier, S. Petitgirard, C. J. Pickard, P. F. McMillan, and M. Mezouar, "Dense close-packed phase of tin above 157 GPa observed experimentally via angle-dispersive X-ray diffraction," Physical Review B **84** (2011), 10.1103/PhysRevB.84.140104.

[5] A. Salamat, R. Briggs, P. Bouvier, S. Petitgirard, A. Dewaele, M. E. Cutler, F. Corà, D. Daisenberger, G. Garbarino, and P. F. McMillan, "High-pressure structural transformations of Sn up to 138 GPa: Angle-dispersive synchrotron X-ray diffraction study," Physical Review B **88** (2013), 10.1103/PhysRevB.88.104104.

[6] A. Lazicki, J. R. Rygg, F. Coppari, R. Smith, D. Fratanduono, R. G. Kraus, G. W. Collins, R. Briggs, D. G. Braun, D. C. Swift, and J. H. Eggert, "X-ray diffraction of solid tin to 1.2 TPa," Physical Review Letters **115** (2015), 10.1103/PhysRevLett.115.075502.

[7] S. Desgreniers, Y. K. Vohra, and A. L. Ruoff, "Tin at high pressure: An energy-dispersive X-ray-diffraction study to 120 GPa," Physical Review B **39**, 15 (1989).

[8] H. Mark and M. Polanyi, "Die gitterstruktur, gleitrichtungen und gleitebenen des weißen zinns," Zeitschrift für Physik **18**, 75–96 (1923).

[9] H. Mark and M. Polanyi, "Zur gitterstruktur des weißien zinns," Zeitschrift für Physik **22**, 200 (1924).

[10] P. W. Bridgman, "Some properties of single metal crystals," Proceedings of the National Academy of Sciences **10** (1924).

[11] S. C. Prasad and W. A. Wooster, "The study of the elastic constants of white tin by diffuse X-ray reflexion," Acta Crystallographica **8**, 682–686 (1955).

[12] W. P. Mason and H. E. Bommel, "Ultrasonic attenuation at low temperatures for metals in the normal and superconducting states," Journal of the Acoustical Society of America **28**, 930–943 (1956).

[13] D. G. House and E. V. Vernon, "Determination of the elastic moduli of tin single crystals, and their variation with temperature," British Journal of Applied Physics **11**, 254 (1960).

[14] J. A. Rayne and B. S. Chandrasekhar, "Elastic constants of β tin from 4.2°k to 300°k," Physical Review **120**, 1658–1663 (1960).

[15] L. C. Cardinal, "Report of NRL progress, March 1963," (U. S. Naval Research Laboratory, 1963) Chap. Vibro Analysis of Material, pp. 31–32.

[16] E. W. Kammer, L. C. Cardinal, C. L. Vold, and M. E. Glicksman, "The elastic constants for single-crystal bismuth and tin from room temperature to the melting point," Journal of Physics and Chemistry of Solids **33**, 1891–1892 (1972).

[17] V. T. Deshpande and D. B. Sirdesmukh, "Thermal expansion of tetragonal tin," Acta Crystallographica **14**, 355–356 (1961).

[18] C. B. G. and S. Weintroub, "The measurement of the thermal expansion of single crystals of tin by an interferometric method," Proceedings of the Physical Society. Section B **63**, 267–277 (1950).

[19] M. Straumanis and A. Ievinš, "Die bestimmung von ausdehnungskoeffizienten nach der pulver- und der drehkristall-methode," Zeitschrift für anorganische und allgemeine Chemie **238**, 175–188 (1938).

[20] G. F. Kossolapow and A. K. Trapesnikow, "Struktubericht Band IV," (Akademische Verlagsgesellschaft M.B.H. Leipzig, 1936) Chap. Zinn, Sn: Röntgenographische Bestimmung der thermischen Ausdehnungskoeffizienten von Beryllium und Zinn. Z. Kristallogr. (A) 94 (1936) 53-59, p. 88.

[21] G. Shinoda, "X-ray investigations on the thermal expansions of solids," Memoirs of the College of Science, Kyoto Imperial University, Series A **16**, 193–201 (1933).

[22] G. I. Kirichenko, "Anisotropy of plastic deformation of tin single crystals in the temperature range 4.2-300K," The Physics of Metals and Metallography **63**, 144–151 (1987).

[23] J. Obinata and E. Schmid, "Über die dehnung von zinnkristallen." Zeitschrift für Physik **82**, 224–234 (1933).

[24] K. Bausch, "Untersuchung der schiebegleitung an zinneinkristallen," Zeitschrift für Physik **93**, 476–509 (1935).

[25] J. Weertman and J. E. Breen, "Creep of tin single crystals," Journal of Applied Physics **27**, 1189–1193 (1956).

[26] R. W. Vook, "Dislocations in evaporated single crystal tin films," Acta Metallurgica **12**, 197–207 (1964).

[27] O. Brümmer and V. Alex, "Züchtung, präparation und Röntgentopographie nahezu idealer Sn-kristalle," physica status solidi (a) **3**, 193–199 (1970).

[28] R. Fiedler and A. R. Lang, "Dislocation generation at surfaces of tin single crystals," Journal of Materials Science **7**, 531–542 (1972).

[29] K. Honda, "Configurations, formation and burgers vector of coupled dislocations straddling a polygon wall in white tin single crystals," Japanese Journal of Applied Physics **17**, 33–41 (1978).

[30] K. Honda, "Dislocation walls consisting of double arrays in white tin single crystals," Japanese Journal of Applied Physics **18**, 215–224 (1979).

[31] K. Ojima and T. Hirokawa, "Motions of individual dislocations in white tin single crystals deformed in tension," Japanese Journal of Applied Physics **22**, 46–51 (1983).

[32] K. Honda, "Dislocation reactions in a boundary of a white tin crystal," Japanese Journal of Applied Physics **26**, 637–638 (1987).

[33] M. Nagasaka, "Temperature dependence of plastic deformation in white tin single crystals," Japanese Journal of Applied Physics **28**, 446–452 (1989).

[34] B. Düzgün and I. Aytaş, "Investigation of operative slip system in β-Sn single crystal and the relation between the crystal orientation and the slip systems," Japanese Journal of Applied Physics **32**, 3214–3216 (1993).

[35] B. Düzgün, N. Uçar, and S. I. Aytaş, "The dislocation movement in white tin single crystals," Turkish Journal of Physics **20**, 459–464 (1996).

[36] B. Düzgün and N. Uçar, "The relation between dislocation density and crystal crosscut in β-Sn grown by modified bridgman method," Turkish Journal of Physics **22**, 803–809 (1998).

[37] M. Fujiwara and T. Hirokawa, "The strength of main obstacles to dislocation motion in white tin crystals," Journal of the Japan Institute of Metals **51**, 830–836 (1987), [in Japanese].

[38] T. R. Bieler and A. U. Telang, "Analysis of slip behavior in a single shear lap lead-free solder joint during simple shear at 25°C and 0.1/s," Journal of Electronic Materials **38**, 2694–2701 (2009).

[39] B. Chalmers, "The twinning of single crystals of tin," Proceedings of the Physical Society **47** (1935).

[40] S. Maruyama and H. Kiho, "Intersections of {301}, {101} twin bands in tin," Journal of the Physical Society of Japan **11**, 516–521 (1956).

[41] K. Ishii, "Deformation twinning of tin single crystals under impact loading," Journal of the Physical Society of Japan **14**, 1315–1321 (1959).

[42] R. A. Stager, A. S. Balchan, and H. G. Drickamer, "High-pressure phase transition in metallic tin," The Journal of Chemical Physics **37**, 1154 (1962).

[43] R. N. Jeffery, J. D. Barnett, H. B. Vanfleet, and H. T. Hall, "Pressure calibration to 100 kbar based on the compression of NaCl," Journal of Applied Physics **37**, 3172–3180 (1966).

[44] J. D. Barnett, V. E. Bean, and H. T. Hall, "X-ray diffraction studies on tin to 100 kilobars," Journal of Applied Physics **37**, 875–877 (1966).

[45] A. Ohtani, M. Seishiro, M. Katayama, A. Onodera, and N. Kawai, "Multi-anvil apparatus for high pressure X-ray diffraction," Japanese Journal of Applied Physics **16**, 1843–1848 (1977).

[46] H. Olijnyk and W. Holzapfel, "Phase transitions in Si, Ge and Sn under pressure," Journal de Physique Colloques **45**, 153–156 (1984).

[47] M. Liu and L. Liu, "Compressions and phase transitions of tin to half a megabar," High Temperatures - High Pressures **18**, 79–85 (1986).

[48] H. D. Stromberg and D. R. Stephens, "Effects of pressure on the electrical resistance of certain metals," Journal of Physics and Chemistry of Solids **25**, 1015–1022 (1964).

[49]J. D. Barnett, R. B. Bennion, and H. T. Hall, "X-ray diffraction studies on tin at high pressure and high temperature," Science **141**, 1041–1042 (1963).

[50]G. C. Kennedy and R. C. Newton, "Solids under pressure," (McGraw-Hill Book Company, Inc., 1963) Chap. Solid-liquid and solid-solid phase transitions in some pure metals at high temperatures and pressures, pp. 163–178.

[51]A. I. Kingon and J. B. Clark, "A redetermination of the melting curve of tin to 3.7 GPa," High Temperatures - High Pressures **12**, 75–79 (1980).

[52]L. Xu, Y. Bi, X. Li, Y. Wang, X. Cao, L. Cai, Z. Wang, and C. Meng, "Phase diagram of tin determined by sound velocity measurements on multi-anvil apparatus up to 5 GPa and 800 K," Journal of Applied Physics **115** (2014), 10.1063/1.4872458.

[53]R. E. Duff, W. H. Gust, E. B. Royce, M. Ross, A. C. Mitchell, R. N. Keeler, and W. G. Hoover, "Shock-wave studies in condensed matter," in *Comportement des Milieux Denses sous Hautes Pressions Dynamiques / Behaviour of Dense Media under High Dynamic Pressures* (1968) pp. 397–406.

[54]R. Courchinoux, P. Chapron, and P. Elias, "Particle velocity profiles measured by LDI through a LiF window in loading-unloading experiments," in *Shock Compression of Condensed Matter 1991*, edited by S. C. Schmidt, R. D. Dick, J. W. Forbes, and D. G. Tasker (1992) pp. 771–774.

[55]M. N. Pavlovskiĭ and V. V. Komissarov, "Polymorphic transitions of tin in shock compression and dilatation waves," Soviet Physics JETP **71** (1990).

[56]T. Chong, J. Mo, H. Fu, T. Li, and B. Luo, "Phase transition and spall behavior of tin under ramp wave compression," Lixue Xuebao/Chinese Journal of Theoretical and Applied Mechanics **55**, 113–119 (2023), [in Chinese].

[57]J.-P. Davis and D. B. Hayes, "Measurement of the dynamic β-γ phase boundary in tin," in *Shock Compression of Condensed Matter - 2007*, Vol. 955 (2007) pp. 159–162.

[58]R. Fréville, A. Dewaele, N. Guignot, P. Faure, L. Henry, G. Garbarino, and M. Mezouar, "High-pressure-high-temperature phase diagram of tin," Physical Review B **109** (2024), 10.1103/PhysRevB.109.104116.

[59]C. Mabire and P. L. Héreil, "Shock induced polymorphic transition and melting of tin," in *Shock Compression of Condensed Matter - 1999*, Vol. 505 (AIP Publishing, 2000) pp. 93–96.

[60]C. Chauvin, J. Petit, and F. Sinatti, "Polymorphic transition of tin under shock wave compression: Experimental results," in *DYMAT 2012*, Vol. 26 (2012).

[61]R. Briggs, R. Torchio, A. Sollier, F. Occelli, L. Videau, N. Kretzschmar, and M. Wulff, "Observation of the shock-induced β-Sn to b.c.t.-Sn transition using time-resolved X-ray diffraction," Journal of Synchrotron Radiation **26**, 96–101 (2019).

[62]C. Chauvin, F. Zucchini, and D. P. de Barros, "Study on phase transformation in tin under dynamic compression," in *Proceedings of the 2019 Hypervelocity Impact Symposium* (2019).

[63]W. W. Anderson, F. Cverna, R. S. Hixson, J. Vorthman, M. D. Wilke, G. T. I. Gray, and K. L. Brown, "Phase transition and spall behavior in β-tin," in *Shock Compression of Condensed Matter - 1999* (AIP Publishing, 2000) pp. 443–446.

[64]G. A. Cox and C. M. Robinson, "Empirical multi-phase EoS modelling issues," in *Shock Compression of Condensed Matter - 2009*, Vol. 1195 (2009) pp. 1195–1200.

[65]C. Mabire, *Transformation polymorphique et fusion de l'étain sous choc dans la gamme 0-100 GPa; étude expérimentale et modélisation*, Ph.D. thesis, Université de Poitiers (1999).

[66]J. D. Dudley and H. T. Hall, "Experimental fusion curves of indium and tin to 105 000 atmospheres," Physical Review **118**, 1211–1216 (1960).

[67]S. D. Gilev and V. S. Prokop'ev, "Electrical resistance of high-pressure phases of tin under shock compression," Combustion, Explosion and Shock Waves **51**, 482–487 (2015).

[68]L. Soulard and O. Durand, "Observation of phase transitions in shocked tin by molecular dynamics," Journal of Applied Physics **127** (2020), 10.1063/5.0003089.

[69]M. T. Beason and B. J. Jensen, "Constraining the release of Sn to the ambient melting point following shock loading using time-resolved X-ray diffraction," Journal of Applied Physics **132** (2022), 10.1063/5.0128101.

[70]D. B. Bober, J. Lind, A. M. Saunders, and M. C. Akin, "X-ray diffraction from shock driven Sn microjets," Journal of Applied Physics **132** (2022), 10.1063/5.0111216.

[71]C. Chauvin, D. P. de Barros, A. Delaunay, and T. D. Rességuier, "Coupling a gas gun with an X-pinch x-ray source to perform x-ray diffraction under shock loading," Review of Scientific Instruments **96** (2025), 10.1063/5.0245052.

[72]D. B. Bober, K. K. Mackay, M. C. Akin, and F. M. Najjar, "Understanding the evolution of liquid and solid microjets from grooved Sn and Cu samples using radiography," Journal of Applied Physics **130** (2021), 10.1063/5.0056245.

[73]W. S. Vogan, W. W. Anderson, M. Grover, J. E. Hammerberg, N. S. King, S. K. Lamoreaux, G. MacRum, K. B. Morley, P. A. Rigg, G. D. Stevens, W. D. Turley, L. R. Veeser, and W. T. Buttler, "Piezoelectric characterization of ejecta from shocked tin surfaces," Journal of Applied Physics **98** (2005), 10.1063/1.2132521.

[74]M. B. Zellner, M. Grover, J. E. Hammerberg, R. S. Hixson, A. J. Iverson, G. S. MacRum, K. B. Morley, A. W. Obst, R. T. Olson, J. R. Payton, P. A. Rigg, N. Routley, G. D. Stevens, W. D. Turley, L. Veeser, and W. T. Buttler, "Effects of shock-breakout pressure on ejection of micron-scale material from shocked tin surfaces," Journal of Applied Physics **102** (2007), 10.1063/1.2752130.

[75]M. B. Zellner, W. V. McNeil, G. T. Gray, D. C. Huerta, N. S. King, G. E. Neal, S. J. Valentine, J. R. Payton, J. Rubin, G. D. Stevens, W. D. Turley, and W. T. Buttler, "Surface preparation methods to enhance dynamic surface property measurements of shocked metal surfaces," Journal of Applied Physics **103** (2008), 10.1063/1.2906107.

[76]M. B. Zellner, W. V. McNeil, J. E. Hammerberg, R. S. Hixson, A. W. Obst, R. T. Olson, J. R. Payton, P. A. Rigg, N. Routley, G. D. Stevens, W. D. Turley, L. Veeser, and W. T. Buttler, "Probing the underlying physics of ejecta production from shocked Sn samples," Journal of Applied Physics **103** (2008), 10.1063/1.2939253.

[77]S. K. Monfared, D. M. Oró, M. Grover, J. E. Hammerberg, B. M. Lalone, C. L. Pack, M. M. Schauer, G. D. Stevens, J. B. Stone, W. D. Turley, and W. T. Buttler, "Experimental observations on the links between surface perturbation parameters and shock-induced mass ejection," Journal of Applied Physics **116** (2014), 10.1063/1.4891449.

[78]T. D. Rességuier, E. Lescoute, A. Sollier, G. Prudhomme, and P. Mercier, "Microjetting from grooved surfaces in metallic samples subjected to laser driven shocks," Journal of Applied Physics **115** (2014), 10.1063/1.4863719.

[79]R. A. Meijer, R. Schupp, J. Sheil, M. M. Basko, K. S. Eikema, O. O. Versolato, and S. Witte, "Spall-velocity reduction in double-pulse impact on tin microdroplets," Physical Review Applied **16** (2021), 10.1103/PhysRevApplied.16.024026.

[80]M. J. P. Musgrave, "On the transition from white tin (β) to the body-centred cubic form under pressure," Journal of Physics and Chemistry of Solids **24**, 557–558 (1963).

[81]H. Katzke and P. Tolédano, "Structural mechanisms of the high-pressure phase transitions in the elements of group IVa," Journal of Physics Condensed Matter **19** (2007), 10.1088/0953-8984/19/27/275204.

[82]R. Fréville, *Transitions de phase et microstructures induites dans les métaux en conditions extrêmes : fer et étain*, Ph.D. thesis, Université Paris-Saclay (2023).

[83]M. S. Nitol, K. Dang, S. J. Fensin, M. I. Baskes, D. E. Dickel, and C. D. Barrett, "Hybrid interatomic potential for Sn," Physical Review Materials **7** (2023), 10.1103/PhysRevMaterials.7.043601.

[84]W. S. Ko, D. H. Kim, Y. J. Kwon, and M. H. Lee, "Atomistic simulations of pure tin based on a new modified embedded-atom method interatomic potential," Metals **8** (2018), 10.3390/met8110900.

[85]M. I. Baskes, "Modified embedded-atom potentials for cubic materials and impurities," Physical Review B **46** (1992).

[86]R. Ravelo and M. Baskes, "Equilibrium and thermodynamic properties of grey, white, and liquid tin," Physical Review Letters **79**, 2482–2485 (1997).

[87]R. S. Elliott and A. Akerson, "Efficient "universal" shifted Lennard-Jones model for all KIM API supported species," (2015).

[88]T. Chen, F. Yuan, J. Liu, H. Geng, L. Zhang, H. Wang, and M. Chen, "Modeling the high-pressure solid and liquid phases of tin from deep potentials with ab initio accuracy," Physical Review Materials **7** (2023), 10.1103/PhysRevMaterials.7.053603.

[89]F. A. Sapozhnikov, G. V. Ionov, V. V. Dremov, L. Soulard, and O. Durand, "The embedded atom model and large-scale MD simulation of tin under shock loading," in *Journal of Physics: Conference Series*, Vol. 500 (Institute of Physics Publishing, 2014).
[90]J. R. Vella, M. Chen, F. H. Stillinger, E. A. Carter, P. G. Debenedetti, and A. Z. Panagiotopoulos, "Structural and dynamic properties of liquid tin from a new modified embedded-atom method force field," Physical Review B **95** (2017), 10.1103/PhysRevB.95.064202.
[91]J. G. Threadingham, X. Liang, J. C. F. Millett, G. Whiteman, D. J. Chapman, and D. E. Eakins, "Demonstration of a telecentric lens relay system for PDV in plate-impact experiments," in *23rd Biennial Conference of the APS Topical Group on Shock Compression of Condensed Matter*, Vol. 3066 (2024) p. 450015.
[92]O. T. Strand, D. R. Goosman, C. Martinez, T. L. Whitworth, and W. W. Kuhlow, "Compact system for high-speed velocimetry using heterodyne techniques," Review of Scientific Instruments **77** (2006), 10.1063/1.2336749.
[93]O. T. Strand, L. V. Berzins, D. R. Goosman, W. W. Kuhlow, P. D. Sargis, and T. L. Whitworth, "Velocimetry using heterodyne techniques," in *26th International Congress on High-Speed Photography and Photonics*, Vol. 5580 (SPIE, 2005) p. 593.
[94]L. M. Barker and R. E. Hollenbach, "Shock wave study of the $\alpha \rightleftarrows \varepsilon$ phase transition in iron," Journal of Applied Physics **45**, 4872–4887 (1974).
[95]W. H. Gust and E. B. Royce, "Axial yield strengths and two successive phase transition stresses for crystalline silicon," Journal of Applied Physics **42**, 1897–1905 (1971).
[96]J. M. Walsh and R. H. Christian, "Equation of state of metals from shock wave measurements," Physical Review **97**, 1544–1556 (1955).
[97]G. E. Duvall and R. A. Graham, "Phase transitions under shock-wave loading," Reviews of Modern Physics **Vol**, 523–579 (1997).
[98]S. P. Marsh, "LASL shock Hugoniot data," Tech. Rep. (1980).
[99]M. van Thiel, "Compendium of shock wave data," Tech. Rep. (1977).
[100]J. M. Walsh, M. H. Rice, R. G. Mcqueen, and F. L. Yarger, "Shock-wave compressions of twenty-seven metals. Equations of state of metals," Physical Review **108** (1957), 10.1103/PhysRev.108.196.
[101]L. V. Al'tshuler, K. K. Krupnikov, and M. I. Brazhnik, "Dynamical compressibility of metals under pressure from 400,000 to 4,000,000 atmospheres," Soviet Physics JETP **34** (1958).
[102]L. V. Al'tshuler, A. A. Bakanova, and R. F. Trunin, "Shock adiabats and zero isotherms of seven metals at high pressures," Soviet Physics JETP **15**, 65–74 (1962).
[103]K. V. Volkov and V. A. Sibilev, "Investigation of the shock compression of liquid tin at pressures up to 100 gpa and initial temperatures of 310... 475°c," Journal of Applied Mechanics and Technical Physics **22**, 551–558 (1981).
[104]D. J. Steinberg, "Equation of state and strength properties of selected materials," Tech. Rep. (1996).
[105]E. Moshe, S. Eliezer, E. Dekel, Z. Henis, A. Ludmirsky, I. B. Goldberg, and D. Eliezer, "Measurements of laser driven spallation in tin and zinc using an optical recording velocity interferometer system," Journal of Applied Physics **86**, 4242–4248 (1999).
[106]T. de Rességuier, L. Signor, A. Dragon, P. Severin, and M. Boustie, "Spallation in laser shock-loaded tin below and just above melting on release," Journal of Applied Physics **102** (2007), 10.1063/1.2795436.
[107]K. D. Swartz, W. B. Chua, and C. Elbaum, "Third-order elastic constants of tin and of a tin-indium alloy," Physical Review B **6**, 426–435 (1972).
[108]R. S. McWilliams, *Elastic and Inelastic Shock Compression of Diamond and Other Minerals*, Ph.D. thesis, University of California (2008).
[109]W. J. Schill, J. Lind, J. L. Brown, M. B. Prime, S. J. Fensin, D. R. Jones, D. T. Martinez, J. W. Dyer, T. T. Nguyen, M. Nelms, K. L. Schmidt, C. C. Bataile, J. M. Lane, and N. R. Barton, "A surprising proliferation of detwinning in β-tin at extreme loading rates," Scripta Materialia **264** (2025), 10.1016/j.scriptamat.2025.116727.
[110]R. Fiedler and I. Vagera, "On the Burgers vectors in β-Sn single crystals," Physica Status Solidi (a) **32**, 419–424 (1975).
[111]P. Darbandi, T. R. Bieler, F. Pourboghrat, and T. K. Lee, "Crystal plasticity finite-element analysis of deformation behavior in multiple-grained lead-free solder joints," Journal of Electronic Materials **42**, 201–214 (2013).
[112]F. Yang and J. C. Li, "Deformation behavior of tin and some tin alloys," Journal of Materials Science: Materials in Electronics **18**, 191–210 (2007).
[113]A. U. Telang and T. R. Bieler, "The orientation imaging microscopy of lead-free Sn-Ag solder joints," Journal of the Minerals, Metals & Materials Society **57**, 44–49 (2005).
[114]G. I. Kanel, S. V. Razorenov, A. V. Utkin, and D. E. Grady, "The spall strength of metals at elevated temperatures," in *Shock Compression of Condensed Matter - 1995* (AIP Publishing, 1996) pp. 503–506.
[115]D. V. Morgan, M. Grover, D. Macy, M. Madlener, G. Stevens, and W. D. Turley, "Observations of shock-loaded tin and zirconium surfaces with single-pulse X-ray diffraction," Powder Diffraction **25**, 138–142 (2010).
[116]T. Nguyen, L. Burakovsky, S. J. Fensin, D. J. Luscher, M. B. Prime, C. Cady, G. T. Gray, D. R. Jones, D. T. Martinez, R. L. Rowland, S. Sjue, B. T. Sturtevant, and J. A. Valdez, "Calibration and validation of the foundation for a multiphase strength model for tin," Journal of Applied Physics **135** (2024), 10.1063/5.0207405.

Appendix A: Calculating Resolved Shear Stress

The shear on the slip plane is given by

$$\tau = \hat{\mathbf{d}} \cdot (\boldsymbol{\sigma} \cdot \hat{\mathbf{m}}), \tag{A1}$$

The stress field $\boldsymbol{\sigma}$ can be determined using the aforementioned third order model, assuming one dimensional strain. The principal components for each orientation are given by

$$\sigma_1 = -\frac{v}{v_0}\eta\left(C_{11} + \frac{\eta}{2}C_{111}\right), \tag{A2a}$$
$$\sigma_2 = -\frac{v}{v_0}\eta\left(C_{12} + \frac{\eta}{2}C_{112}\right), \tag{A2b}$$
$$\sigma_3 = -\frac{v}{v_0}\eta\left(C_{13} + \frac{\eta}{2}C_{113}\right), \tag{A2c}$$

for orientation (100);

$$\sigma_1 = -\frac{v}{v_0}\eta\left(C_{13} + \frac{\eta}{2}C_{133}\right), \tag{A3a}$$
$$\sigma_2 = -\frac{v}{v_0}\eta\left(C_{13} + \frac{\eta}{2}C_{133}\right), \tag{A3b}$$
$$\sigma_3 = -\frac{v}{v_0}\eta\left(C_{33} + \frac{\eta}{2}C_{333}\right), \tag{A3c}$$

for orientation (001); and

$$\sigma_1 = \sigma_2 = -\frac{v}{v_0}\frac{\eta}{2}\left((C_{11}+C_{12}) + \frac{\eta}{4}(C_{111}+3C_{112}) + \eta C_{166}\right), \tag{A4a}$$
$$\sigma_6 = -\frac{v}{v_0}\eta\left(C_{66} + \eta C_{166}\right), \tag{A4b}$$
$$\sigma_3 = -\frac{v}{v_0}\frac{\eta}{2}\left(2C_{13} + \frac{\eta}{4}(2C_{113}+3C_{123}) + \eta C_{366}\right), \tag{A4c}$$

for (110), where all other terms are zero and η is defined in equation 8. Using the mean volumetric strain for each orientation from Table I $\left((v/v_0)_{(100)} = 0.933,\ (v/v_0)_{(001)} = 0.984,\ (v/v_0)_{(100)} = 0.993\right)$, the second order parameters from Rayne and Chandrasekhar[14] and the third order parameters from Swartz *et al.*[107] yields

$$\boldsymbol{\sigma}_{\mathbf{100}} = \begin{bmatrix} -5.17 & 0 & 0 \\ 0 & -4.73 & 0 \\ 0 & 0 & -3.08 \end{bmatrix} \text{GPa}, \tag{A5a}$$

$$\boldsymbol{\sigma}_{\mathbf{001}} = \begin{bmatrix} -0.62 & 0 & 0 \\ 0 & -0.62 & 0 \\ 0 & 0 & -1.56 \end{bmatrix} \text{GPa}, \tag{A5b}$$

and

$$\boldsymbol{\sigma}_{\mathbf{110}} = \begin{bmatrix} -0.47 & -0.18 & 0 \\ -0.18 & -0.47 & 0 \\ 0 & 0 & -0.25 \end{bmatrix} \text{GPa}. \tag{A5c}$$

The slip plane normal and slip direction are then given by

$$\hat{\mathbf{d}} = \frac{1}{\sqrt{(ua_1)^2 + (va_2)^2 + (wc_3)^2}} \begin{bmatrix} ua_1 \\ va_2 \\ wc_3 \end{bmatrix} \tag{A6a}$$

and

$$\hat{\mathbf{m}} = \frac{1}{\sqrt{\left(\frac{h}{a_1}\right)^2 + \left(\frac{k}{a_2}\right)^2 + \left(\frac{l}{c_3}\right)^2}} \begin{bmatrix} \frac{h}{a_1} \\ \frac{k}{a_2} \\ \frac{l}{c_3} \end{bmatrix}. \tag{A6b}$$

where (h,k,l) and $[u,v,w]$ have their usual crystallographic meaning and are tabulated in Table IV. Due to the large strains, especially in the (100) orientation, the strained lattice parameters are used. Assuming one dimensional strain, for (100) $a_1 = a\frac{v}{v_0}, a_2 = a$ and $c_3 = c$, while for (001) $c_3 = c\frac{v}{v_0}$ and $a_1 = a_2 = a$. The loading case for (110) is more complicated, with the stretch field

$$\mathbf{F}' = \begin{bmatrix} \frac{v}{v_0} & 0 & 0 \\ 0 & 1 & 0 \\ 0 & 0 & 1 \end{bmatrix} \tag{A7}$$

transformed into Cartesian coordinates using

$$\mathbf{F} = \mathbf{R}^T \mathbf{F}' \mathbf{R} \tag{A8}$$

where

$$\mathbf{R} = \begin{bmatrix} \cos(45) & \sin(45) & 0 \\ -\sin(45) & \cos(45) & 0 \\ 0 & 0 & 1 \end{bmatrix} \tag{A9}$$

to give unit cell parameters

$$\begin{bmatrix} a_1 \\ a_2 \\ c_3 \end{bmatrix} = \mathbf{F} \begin{bmatrix} a \\ a \\ c \end{bmatrix}. \tag{A10}$$

Unstrained lattice parameters $a = 5.8318\,\text{Å}$ and $c = 3.1819\,\text{Å}$ are taken from Deshpande and Sirdesmukh[17].